IJMMM International Journal of Minerals, Metallurgy and Materials 矿物冶金与材料学报（英文版）

Three-dimensional antimony sulfide anode with carbon nanotube interphase modified for lithium-ion batteries

Qi Wang, Yue-yong Du, Yan-qing Lai, Fang-yang Liu, Liang-xing Jiang, and Ming Jia

Cite this article as:
Qi Wang, Yue-yong Du, Yan-qing Lai, Fang-yang Liu, Liang-xing Jiang, and Ming Jia, Three-dimensional antimony sulfide anode with carbon nanotube interphase modified for lithium-ion batteries, *Int. J. Miner. Metall. Mater.*, 28(2021), No. 10, pp. 1629-1635. https://doi.org/10.1007/s12613-021-2249-7

International Journal of Minerals, Metallurgy and Materials
Volume 28, Number 10, October 2021, Page 1629
https://doi.org/10.1007/s12613-021-2249-7

Three-dimensional antimony sulfide anode with carbon nanotube interphase modified for lithium-ion batteries

Qi Wang, Yue-yong Du, Yan-qing Lai, Fang-yang Liu, Liang-xing Jiang, and Ming Jia

School of Metallurgy and Environment, Central South University, Changsha 410083, China
(Received: 24 September 2020; revised: 7 January 2021; accepted: 9 January 2021)

Abstract: Antimony sulfide (Sb_2S_3) is a promising anode for lithium-ion batteries due to its high capacity and vast reserves. However, the low electronic conductivity and severe volume change during cycling hinder its commercialization. Herein our work, a three-dimensional (3D) Sb_2S_3 thin film anode was fabricated via a simple vapor transport deposition system by using natural stibnite as raw material and stainless steel fiber-foil (SSF) as 3D current collector, and a carbon nanotube interphase was introduced onto the film surface by a simple dropping-heating process to promote the electrochemical performances. This 3D structure can greatly improve the initial coulombic efficiency to a record of 86.6% and high reversible rate capacity of 760.8 $mAh \cdot g^{-1}$ at 10 C. With carbon nanotubes interphase modified, the Sb_2S_3 anode cycled extremely stable with high capacity retention of 94.7% after 160 cycles. This work sheds light on the economical preparation and performance optimization of Sb_2S_3-based anodes.

Keywords: three dimensions; antimony sulfide anode; carbon nanotubes interphase; lithium-ion batteries

1. Introduction

The employment of graphite as anode has encouraged the widespread commercialization of lithium-ion batteries (LIBs) in the fields of portable electronic products and electric vehicles [1–2]. However, with the increasing demand for high energy/power density of energy supplying devices, graphite may fail to meet the need due to its unsatisfied capacity [3]. Antimony sulfide with high specific capacity (946 $mAh \cdot g^{-1}$) and safe working potential has been believed to be one of the most possible candidates and has been widely studied in rechargeable batteries [4–6]. Unfortunately, the low electronic conductivity and severe volume change during the lithiation/delithiation process (Li_3Sb, ~390%) hinder the commercialization of antimony sulfide anode [7]. To solve the above two challenges that antimony sulfide anode encountered, many strategies have been employed, such as constructing nanostructured particles to buffer the volume stress and shorten the Li^+ diffusion length inside Sb_2S_3 particles [8]; combining Sb_2S_3 particles with graphene or hollow carbon sphere to improve the electrical conductivity and accommodate the expansion of active nanoparticles [9–11]. Besides many effective nanostructure designs (such as rod-like and bundle-like Sb_2S_3, ultrathin Sb_2S_3 nanosheet, and so on), thin film anode with nanoscale morphologies (especially three-dimensional structures, 3D) also has a great improvement in cyclic and rate performance. This is because, for one, the active thin film directly deposited on current collector shows strong adhesion to the current collector and eradicates the utilization of inactive binder and conductive agent [12]; for another, the 3D structural film provides larger surface area and thus increases the electrode/electrolyte contact, facilitates Li^+/e^- transport, and enhances the rate capability [13−14]. Moreover, compared to 2D film, 3D film has larger mass loading of active material, better properties in releasing the strain during cycling, which leads to long cycle life with high capacity [15–17]. Therefore, lots of works have focused on the development of 3D alternative anodes, including Si [18], SnO_2 [19], Fe_2O_3 [20], and TiO_2 [21] thin films. However, as to Sb_2S_3 anode, researchers are more interested in the construction of nanostructured particles and Sb_2S_3-carbon composites, limited reports devoted to taking the advantages of the 3D thin films.

In our previous work, we fabricated a 3D amorphous Sb_2S_3 anode by reactive radio frequency magnetron sputtering, which exhibits good electrochemical performance [22]. However, there are still two significant issues that need to be confronted. One issue is that the preparation of thin film is

Corresponding author: Ming Jia E-mail: jiamingsunmoon@aliyun.com

complex and expensive because of the needs of specialized equipment, high purity raw materials, and rigorous process parameters. Another issue is that the large specific area of the electrode is a double-edged sword, which on the other hand leads to high exploration to the electrolyte, resulting in an increased formation of solid-electrolyte interfacial (SEI) layer [23]. Therefore, the process cost, and the destruction/reformation of SEI are crucial issues to address.

Herein our work, a 3D Sb_2S_3 thin film anode was fabricated via a simple vapor transport deposition system by using natural stibnite as raw material and stainless steel fiber-foil (SSF) as 3D current collector, and a carbon nanotubes (CNTs) interphase was introduced onto the film surface (3D Sb_2S_3@CNTs) by a simple dropping-heating method to stabilize the electrode from exfoliation and reduce the depletion of active materials caused by SEI. The depositing system and material used are more feasible and cheaper than the traditional way. Thanks to the modification of CNTs layer, the 3D Sb_2S_3@CNTs shows excellent cycling stability and gives 845 $mAh \cdot g^{-1}$ after 160 cycles with capacity retention of 94.7%. The CNTs layer not only stabilizes the electrode structure but also reduces the depletion of active materials.

2. Experimental

2.1. Chemical and materials

Natural stibnite ore (~95wt% of Sb_2S_3, with main impurities of SiO_2 and Sb_2O_3) was purchased from Hunan Taojiang Banxi Antimony Mine, China. 316L stainless steel fiber foils were purchased from Xinxiang Xinli Filter Tech Co., Ltd., Xinxiang, Henan province, China. Carbon nanotube aqueous dispersion (~6.2wt%) was purchased from Nanjing XFNANO Materials Tech Co., Ltd. (XFNANO). 316L stainless steel fiber foil was used as 3D substrate and washed by deionized water and alcohol in ultrasonic cleaning system before deposition.

2.2. Preparation of 3D Sb_2S_3 thin films

3D Sb_2S_3 thin film was prepared by a vapor transport deposition system that consists of a tubular furnace and a mechanical pump. In a typical preparation process, natural stibnite powder was placed into the heating area of the tube and 3D foil substrates were put into the depositing area, then the tube was sealed and vacuumized to 2 Pa. While depositing, the tube was heated to 495°C with a heating rate of 20°C $\cdot min^{-1}$, and preserved at this temperature for 4 min. The natural stibnite powder was then evaporated and transported to the 3D substrates to get 3D Sb_2S_3 thin films. The mass loading of active material on the substrate is 0.50–0.55 $mg \cdot cm^{-2}$.

2.3. Preparation of 3D Sb_2S_3@CNTs thin films

3D Sb_2S_3@CNTs thin films were prepared by a simple dropping-heating method. Firstly, 0.5 g CNTs aqueous dispersion and 50 mL ethyl alcohol were added into a beaker and well dispersed by ultrasonic treatment to get a CNTs suspension. Secondly, 3D Sb_2S_3 thin films were placed on a heating platform with setting temperature of 100°C, and then CNTs suspension was dropped onto the thin films, after drying, repeated the process for several times to finally obtain CNTs interphase modified 3D Sb_2S_3 thin films. The mass loading of CNTs layer on the 3D Sb_2S_3@CNTs is about 0.05−0.07 $mg \cdot cm^{-2}$.

2.4. Characterization

The crystal structures of 3D Sb_2S_3 and CNTs interphase modified thin films were investigated by X-ray diffraction (XRD, Rigaku3014). The element states and bonds of the above samples were analyzed by X-ray photoelectron spectroscopy (XPS, K_α) and Raman measurements (Jobin-Yvon LabRAM HR800-Horiba spectrometer). The morphologies of the samples were observed by field emission scanning electron microscopy (FE-SEM).

2.5. Assembly of coin cells

CR2025 coin-type cells were assembled in glove box full of argon by using 3D Sb_2S_3 and 3D Sb_2S_3@CNTs thin films as working electrodes and Li foil as the counter and reference electrode. 1 M $LiPF_6$ in a mixed solution of ethylene carbonate, dimethyl carbonate, and ethyl methyl carbonate was employed as electrolyte.

2.6. Electrochemical measurement

The cycling and rate performance of the assembled coin cells were measured in a voltage range of 0.01–3 V with LAND battery test system (CT2001A). Cyclic voltammetry (CV) and electrochemical impedance spectroscopy (EIS) were conducted on a PAST 4000 electrochemical workstation.

3. Results and discussion

The XRD patterns of 3D Sb_2S_3 and 3D Sb_2S_3@CNTs present well crystalline structure of Sb_2S_3 phases (JCPDS No. 42-1393), as shown in Fig. 1(a). Raman spectra in Fig. 1(b) shows that both the two samples reveal obvious Sb_2S_3 bonds (peaks around 300, 280, and 189 cm^{-1}) [24–26]. The 3D Sb_2S_3@CNTs also exhibits Sb_2O_3 (446 and 247 cm^{-1}) [27–28] and carbonaceous bonds (G-band at 1580 cm^{-1} and D-band at 1345 cm^{-1}) [29–30]. The appearance of antimony oxide can be ascribed to the surface oxidation by air in the heating procedure. These results indicate that depositing stibnite ore on the 3D substrate is a feasible and effective method, and the CNTs interlayer on the surface of the 3D film is chemically stable.

X-ray photoelectron spectroscopy (XPS) was employed to analyze the chemical composite and element state of 3D

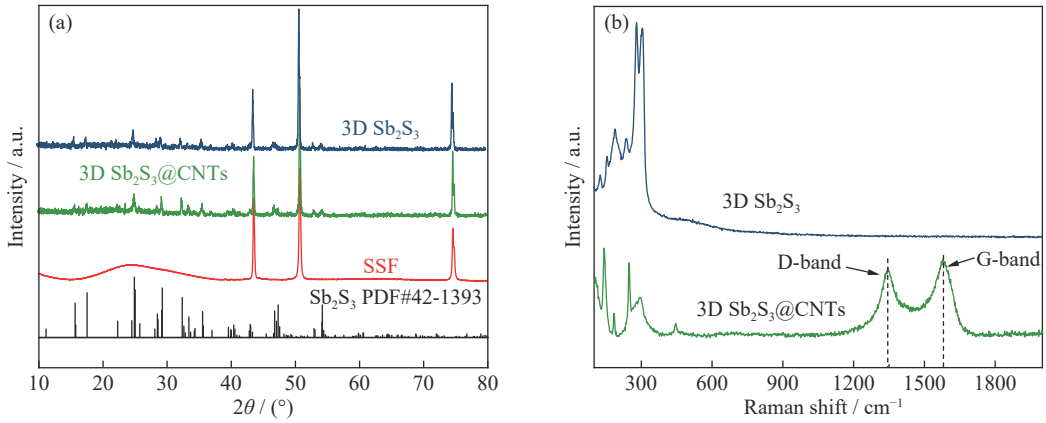

Fig. 1. Characterization of 3D Sb_2S_3 and 3D Sb_2S_3@CNTs thin films: (a) XRD patterns and (b) Raman spectra.

Sb_2S_3@CNTs thin film. Fig. 2(a) shows the XPS full spectrum, giving three elements of Sb, S, and C. The corresponding high resolution spectra of Sb 3d and S 2p are shown in Figs. 2(b) and 2(c) respectively. The Sb 3d peak located at 537.2 and 527.8 eV are belonging to Sb $3d_{3/2}$ and Sb $3d_{5/2}$, indicating the chemical state of Sb^{3+} in the sample [31]. The two peaks at 160.9 and 159.7 eV of S 2p spectra with peak splitting of 1.2 eV are corresponding to S $2p_{1/2}$ and S $2p_{2/3}$, respectively, revealing the surface element state of S^{2-} [32]. The XPS results are in agreement with the analysis of XRD and Raman peaks, confirming the existence of Sb_2S_3 in the 3D Sb_2S_3@CNTs thin film sample.

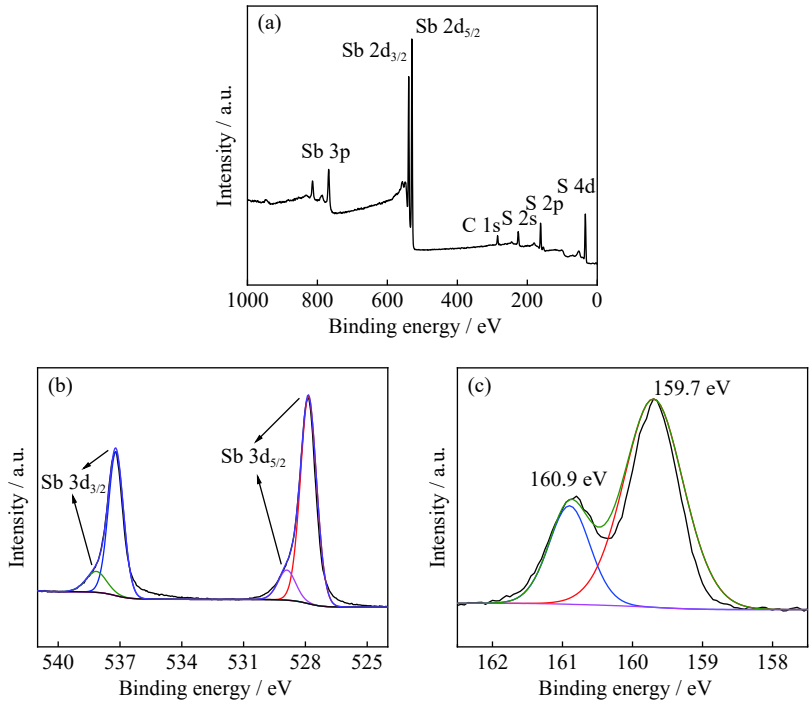

Fig. 2. XPS spectra of 3D Sb_2S_3@CNTs thin film: (a) survey spectrum; (b) Sb 3d spectrum; (c) S 2p spectrum.

The morphologies of the samples were analyzed by scanning electron microscopy (SEM). The Sb_2S_3 thin film on the 3D SSF substrate is formed by connected Sb_2S_3 nanoparticles with particle size of 400–600 nm, as shown in Figs. 3(a)–3(c). The Sb_2S_3 film is uniformly coated on the substrate surface to construct a 3D structure electrode. Besides the abovementioned advantages of 3D electrode, active materials with nanostructure present many merits, such as better accommodation of the stress during lithiation/delithiation, higher electrode/electrolyte contact area, short path way for Li^+/e^- transport inner the electrode, these features will lead to good electrochemical reversibility, fast charge/discharge rate and high capacity of the electrodes [23]. Figs. 3(d)–3(f) show the CNTs network on 3D Sb_2S_3, it can be seen that the CNTs network is transparent and the Sb_2S_3 nanoparticles under the CNTs layer is visible, indicating a CNTs structure stabilizer

is successfully constructed to the 3D Sb_2S_3 thin film electrode. This CNTs layer with pores allows Li^+ to pass through and is flexible and adhesive to the electrode thus avoids Sb_2S_3 from pulverization and reduces the destruction/re-formation of SEI [30].

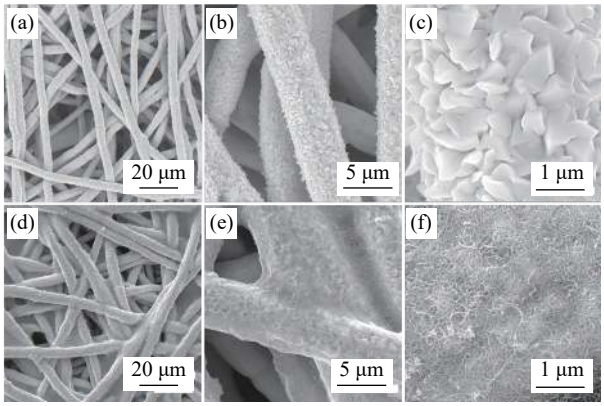

Fig. 3. SEM images of (a–c) 3D Sb_2S_3 thin film and (d–f) 3D Sb_2S_3@CNTs thin film at different magnifications.

CV was conducted to analyze the lithiation and delithiation potentials of the two electrodes. As shown in Fig. 4(a), in lithiation process, two significant cathodic peaks appear at 1.38 and 0.72 V, where 1.38 V is the redox reaction of Sb_2S_3 to Sb and Li_2S, and 0.72 V is the alloying reaction of Sb and Li^+ to form Li_3Sb, respectively. The inverse process shows to anodic peaks at 1.13 and 2.08 V, corresponding to the dealloying of Li_3Sb and oxidation reaction of re-forming Sb_2S_3 [33–34]. After the first scan, the subsequent curves overlap well, indicating high electrochemical reversibility of 3D Sb_2S_3@CNTs electrode. The 3D Sb_2S_3 anode exhibits an initial coulombic efficiency (ICE) of 86.6% and initial discharge capacity of 1113.6 $mAh \cdot g^{-1}$, which is one of the highest coulombic efficiencies reported so far for Sb_2S_3-based anodes. Fig. 4(b) shows the cyclic performance of the two electrodes. The first discharge/charge capacity of 3D Sb_2S_3@CNTs anode is 1225.1 and 891.9 $mAh \cdot g^{-1}$, with a corresponding ICE of 72.8%. The lower ICE and higher capacity of 3D Sb_2S_3@CNTs may be caused by the irreversible side reaction of CNTs layer in the first cycle, because from the second cycle on, the coulombic efficiency of 3D Sb_2S_3@CNTs increased as high as 99.16%, presenting an outstanding reversibility [35]. The 3D Sb_2S_3 cycles stable for the first 50 cycles, giving a high capacity retention of 91.4% (with discharge capacity of 865.1 $mAh \cdot g^{-1}$). However, the capacity fades fast and only 446.3 $mAh \cdot g^{-1}$ last after 160 cycles. Inspiringly, the 3D Sb_2S_3@CNTs anode keeps prominent cycling performance in the whole process, obtaining excellent reversible capacity of 845 $mAh \cdot g^{-1}$ and retention of

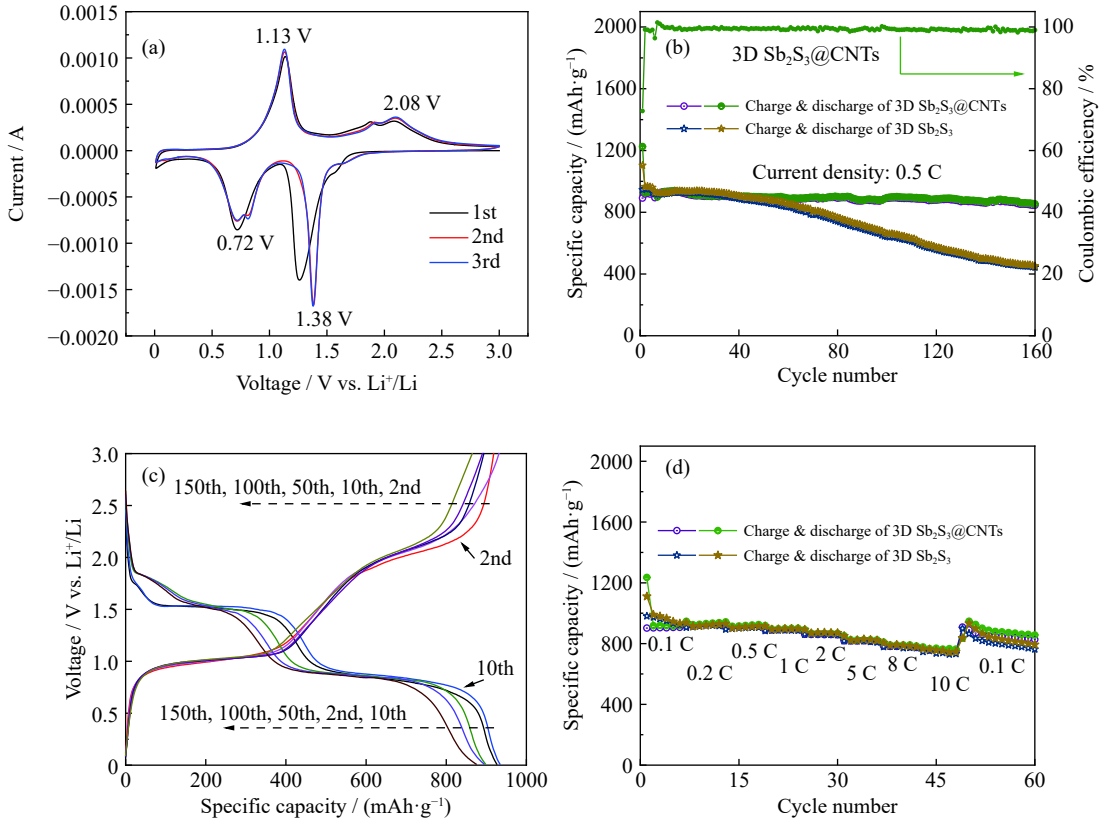

Fig. 4. (a) CV curves of 3D Sb_2S_3@CNTs at scan rate of 0.1 $mV \cdot s^{-1}$; (b) cycling performance of 3D Sb_2S_3 and 3D Sb_2S_3@CNTs; (c) charge/discharge profiles of 3D Sb_2S_3@CNTs; (d) rate performance of the above two samples.

94.7% after 160 cycles. The results verify that the CNTs layer not only stabilizes the electrode structure but also reduces the depletion of active materials, so that after modification the 3D Sb_2S_3 could cycle stable with high capacity. The corresponding charge/discharge profiles of 3D Sb_2S_3@CNTs is shown in Fig. 4(c), it can be seen there is no significant polarization during cycling. The two samples show the same rate performance (Fig. 4(d)), while 3D Sb_2S_3@CNTs presents slightly higher capacities of 861.2, 818.3, 783.8, and 760.8 $mAh \cdot g^{-1}$ at various current densities of 2, 5, 8, and 10 C, respectively. The arresting and glorious rate performance of the two anodes indicates a fast kinetic process of the electrodes.

The Nyquist plots of 3D Sb_2S_3@CNTs anode before and after cycling were obtained by electrochemical impedance spectroscopy (EIS) test (Fig. 5). Both of curves consist of a semicircle at high frequency region and a linear section at low frequency region. The semicircle represents the charge transfer resistance in the electrode/electrolyte interface and the slash relates to the Li^+ diffusion inner the electrode [36]. It is obvious that after 50 cycles, the charge transfer resistance of 3D Sb_2S_3@CNTs is much smaller than the fresh anode, indicating good wettability and improving conductivity of 3D Sb_2S_3@CNTs anode, and thus remarkably enhances the cyclic and fast charge/discharge performances of the electrode [37].

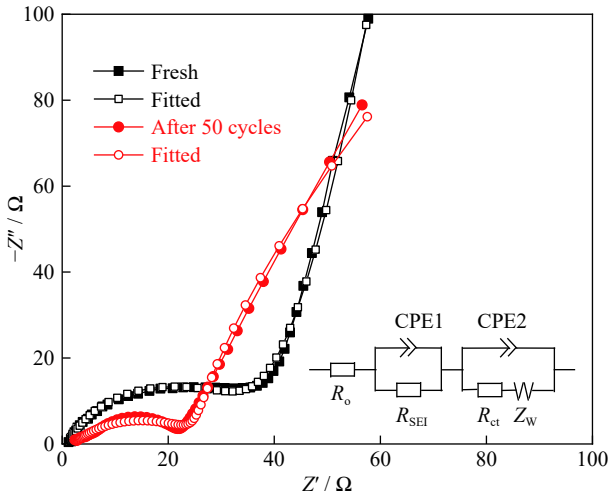

Fig. 5. Nyquist plots of 3D Sb_2S_3@CNTs anode before and after cycling. The insert is the equivalent circuit of the EIS data, where R_o, R_{SEI}, R_{ct}, CPE, and Z_W represents the electrolyte solution resistance, SEI layer resistance, charge transfer resistance, constant phase element, and Warburg impedance, respectively.

SEM analysis was used to investigate the structure stabilities of the two thin film anodes after fifty cycles, as shown in Fig. 6. The SEM images of 3D Sb_2S_3@CNTs at different magnifications (Figs. 6(a) and (b)) prove that the Sb_2S_3-based anodes really suffer from severe volume change during cycling, which generates cracks and electrode expansion. Fortunately, the 3D Sb_2S_3@CNTs maintains its structure stability without active material exfoliation. It could be clearly seen that the CNTs layer on the thin film surface keeps an ultrathin film structure and protects the Sb_2S_3 film from destruction, leading to improved lifespan and reversible capacity [38–39]. On the contrary, after cycling, the 3D Sb_2S_3 on the SSF substrate without CNTs modification encountered structure destruction that the stainless steel fibers are smaller than before, indicating a large amount active Sb_2S_3 lost, so the capacity rapidly decreased.

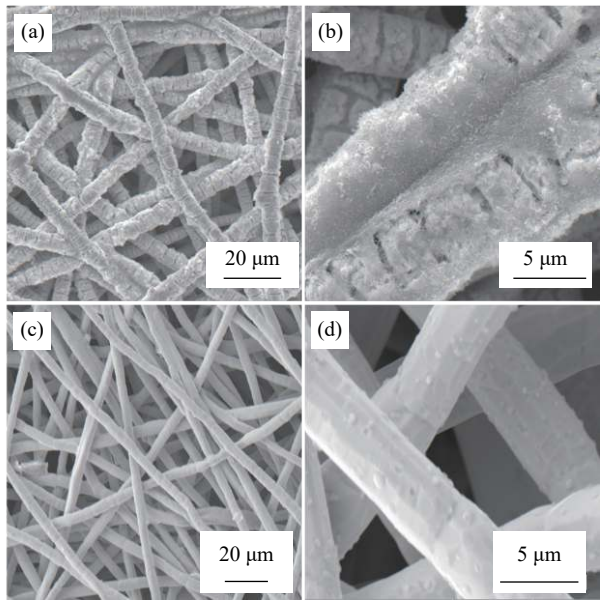

Fig. 6. SEM images of (a, b) cycled 3D Sb_2S_3@CNTs anode and (c, d) cycled 3D Sb_2S_3 anode.

4. Conclusion

In summary, a three-dimensional Sb_2S_3 anode with CNTs interphase modified was successfully constructed via a simple vapor transport deposition system and a simple dropping-heating process. This work shows four superiorities. Firstly, the vapor transport deposition process is fast and shows low energy consumption, which is more feasible and cheaper than the traditional way of Sb_2S_3-based anodes fabrication. Secondly, using natural stibnite as raw material can avoid the conventional metallurgy process, which further reduces the preparation cost and environment pollution. Thirdly, the 3D nanostructure can greatly improve the ICE and rate reversibility of Sb_2S_3 anode, giving a record ICE of 86.6% and high rate capacity of 760.8 $mAh \cdot g^{-1}$ at 10 C, respectively. Lastly, modified by CNTs interphase, the 3D Sb_2S_3 maintains good structure stability and no significant active material exfoliation, obtaining excellent reversible capacity of 845 $mAh \cdot g^{-1}$ and retention of 94.7% after 160 cycles. This work can shed light on the economical prepara-

tion and performance optimization of Sb_2S_3-based anodes.

Acknowledgement

This work was financially supported by the National Natural Science Foundation of China (No. 51774343).

References

[1] M.L. Hao, J. Li, S. Park, S. Moura, and C. Dames, Efficient thermal management of Li-ion batteries with a passive interfacial thermal regulator based on a shape memory alloy, *Nat. Energy*, 3(2018), No. 10, p. 899.

[2] Z.D. Lei, Q.S. Yang, Y. Xu, S.Y. Guo, W.W. Sun, H. Liu, L.P. Lv, Y. Zhang, and Y. Wang, Boosting lithium storage in covalent organic framework via activation of 14-electron redox chemistry, *Nat. Commun.*, 9(2018), art. No. 576.

[3] M. Ko, S. Chae, J. Ma, N. Kim, H.W. Lee, Y. Cui, and J. Cho, Scalable synthesis of silicon-nanolayer-embedded graphite for high-energy lithium-ion batteries, *Nat. Energy*, 1(2016), art. No. 16113.

[4] H.S. Hou, M.J. Jing, Z.D. Huang, Y.C. Yang, Y. Zhang, J. Chen, Z.B. Wu, and X.B. Ji, One-dimensional rod-like Sb_2S_3-based anode for high-performance sodium-ion batteries, *ACS Appl. Mater. Interfaces*, 7(2015), No. 34, p. 19362.

[5] S.H. Dong, C.X. Li, X.L. Ge, Z.Q. Li, X.G. Miao, and L.W. Yin, ZnS–Sb_2S_3@C core-double shell polyhedron structure derived from metal-organic framework as anodes for high performance sodium ion batteries, *ACS Nano*, 11(2017), No. 6, p. 6474.

[6] S.S. Yao, J. Cui, J.Q. Huang, Z.H. Lu, Y. Deng, W.G. Chong, J.X. Wu, M. Ihsan Ul Haq, F. Ciucci, and J.K. Kim, Novel 2D Sb_2S_3 nanosheet/CNT coupling layer for exceptional polysulfide recycling performance, *Adv. Energy Mater.*, 8(2018), No. 24, art. No. 1800710.

[7] W. Luo, X. Ao, Z.S. Li, L. Lv, J.G. Li, G. Hong, Q.H. Wu, and C.D. Wang, Imbedding ultrafine Sb_2S_3 nanoparticles in mesoporous carbon sphere for high-performance lithium-ion battery, *Electrochim. Acta*, 290(2018), p. 185.

[8] S.S. Yao, J. Cui, Y. Deng, W.G. Chong, J.X. Wu, M. Ihsan-Ul-haq, Y.W. Mai, and J.K. Kim, Ultrathin Sb_2S_3 nanosheet anodes for exceptional pseudocapacitive contribution to multi-battery charge storage, *Energy Storage Mater.*, 20(2019), p. 36.

[9] P.V. Prikhodchenko, J. Gun, S. Sladkevich, A.A. Mikhaylov, O. Lev, Y.Y. Tay, S.K. Batabyal, and D.Y.W. Yu, Conversion of hydroperoxoantimonate coated graphenes to Sb_2S_3@Graphene for a superior lithium battery anode, *Chem. Mater.*, 24(2012), No. 24, p. 4750.

[10] X.Z. Zhou, L.H. Bai, J. Yan, S.H. He, and Z.Q. Lei, Solvothermal synthesis of Sb_2S_3/C composite nanorods with excellent Li-storage performance, *Electrochim. Acta*, 108(2013), p. 17.

[11] D.Y.W. Yu, P.V. Prikhodchenko, C.W. Mason, S.K. Batabyal, J. Gun, S. Sladkevich, A.G. Medvedev, and O. Lev, High-capacity antimony sulphide nanoparticle-decorated graphene composite as anode for sodium-ion batteries, *Nat. Commun.*, 4(2013), art. No. 2922.

[12] A.W. Nemaga, J. Mallet, J. Michel, C. Guery, M. Molinari, and M. Morcrette, All electrochemical process for synthesis of Si coating on TiO_2 nanotubes as durable negative electrode material for lithium ion batteries, *J. Power Sources*, 393(2018), p. 43.

[13] J.F. Ni, S.D. Fu, Y.F. Yuan, L. Ma, Y. Jiang, L. Li, and J. Lu, Boosting sodium storage in TiO_2 nanotube arrays through surface phosphorylation, *Adv. Mater.*, 30(2018), No. 6, art. No. 1704337.

[14] R.W. Mo, D. Rooney, K.N. Sun, and H.Y. Yang, 3D nitrogen-doped graphene foam with encapsulated germanium/nitrogen-doped graphene yolk-shell nanoarchitecture for high-performance flexible Li-ion battery, *Nat. Commun.*, 8(2017), art. No. 13949.

[15] H. Park, J.H. Um, H. Choi, W.S. Yoon, Y.E. Sung, and H. Choe, Hierarchical micro-lamella-structured 3D porous copper current collector coated with tin for advanced lithium-ion batteries, *Appl. Surf. Sci.*, 399(2017), p. 132.

[16] R.J. Zou, Z.Y. Zhang, M.F. Yuen, M.L. Sun, J.Q. Hu, C.S. Lee, and W.J. Zhang, Three-dimensional-networked $NiCo_2S_4$ nanosheet array/carbon cloth anodes for high-performance lithium-ion batteries, *NPG Asia Mater.*, 7(2015), No. 6, art. No. e195.

[17] W. Yuan, B.Y. Wang, H. Wu, M.W. Xiang, Q. Wang, H. Liu, Y. Zhang, H.K. Liu, and S.X. Dou, A flexible 3D nitrogen-doped carbon foam@CNTs hybrid hosting TiO_2 nanoparticles as free-standing electrode for ultra-long cycling lithium-ion batteries, *J. Power Sources*, 379(2018), p. 10.

[18] E. Peled, F. Patolsky, D. Golodnitsky, K. Freedman, G. Davidi, and D. Schneier, Tissue-like silicon nanowires-based three-dimensional anodes for high-capacity lithium ion batteries, *Nano Lett.*, 15(2015), No. 6, p. 3907.

[19] H.C. Tao, S.C. Zhu, L.Y. Xiong, X.L. Yang, and L.L. Zhang, Three-dimensional carbon-coated SnO_2/reduced graphene oxide foam as a binder-free anode for high-performance lithium-ion batteries, *ChemElectroChem*, 3(2016), No. 7, p. 1063.

[20] Y. Yang, X.J. Fan, G. Casillas, Z.W. Peng, G.D. Ruan, G. Wang, M.J. Yacaman, and J.M. Tour, Three-dimensional nanoporous Fe_2O_3/Fe_3C-graphene heterogeneous thin films for lithium-ion batteries, *ACS Nano*, 8(2014), No. 4, p. 3939.

[21] S. Moitzheim, J.E. Balder, R. Ritasalo, S. Ek, P. Poodt, S. Unnikrishnan, S. De Gendt, and P.M. Vereecken, Toward 3D thin-film batteries: Optimal current-collector design and scalable fabrication of TiO_2 thin-film electrodes, *ACS Appl. Energy Mater.*, 2(2019), No. 3, p. 1774.

[22] Q. Wang, Y.Q. Lai, F.Y. Liu, L.X. Jiang, and M. Jia, Amorphous Sb_2S_3 anodes by reactive radio frequency magnetron sputtering for high-performance lithium-ion half/full cells, *Energy Technol.*, 7(2019), No. 11, art. No. 1900928.

[23] A.S. Aricò, P. Bruce, B. Scrosati, J.M. Tarascon, and W. Van Schalkwijk, Nanostructured materials for advanced energy conversion and storage devices, *Nat. Mater.*, 4(2005), No. 5, p. 366.

[24] P. Makreski, G. Petruševski, S. Ugarković, and G. Jovanovski, Laser-induced transformation of stibnite (Sb_2S_3) and other structurally related salts, *Vib. Spectrosc.*, 68(2013), p. 177.

[25] P. Makreski, G. Jovanovski, B. Minceva-Sukarova, B. Soptrajanov, A. Green, B. Engelen, and I. Grzetic, Vibrational spectra of $M_3^IM^{III}S_3$ type synthetic minerals (M^I = Tl or Ag and M^{III} = As or Sb), *Vib. Spectrosc.*, 35(2004), No. 1-2, p. 59.

[26] S. Kharbish, E. Libowitzky, and A. Beran, Raman spectra of isolated and interconnected pyramidal XS3 groups (X = Sb, Bi) in stibnite, bismuthinite, kermesite, stephanite and bournonite, *Eur. J. Mineral.*, 21(2009), No. 2, p. 325.

[27] H. Li, K. Qian, X.Y. Qin, D.Q. Liu, R.Y. Shi, A.H. Ran, C.P. Han, Y.B. He, F.Y. Kang, and B.H. Li, The different Li/Na ion storage mechanisms of nano Sb_2O_3 anchored on graphene, *J. Power Sources*, 385(2018), p. 114.

[28] R. Parize, T. Cossuet, O. Chaix-Pluchery, H. Roussel, E. Appert, and V. Consonni, *In situ* analysis of the crystallization process of Sb_2S_3 thin films by Raman scattering and X-ray diffraction, *Mater. Des.*, 121(2017), p. 1.

[29] Q.H. Nguyen, J.S. Choi, Y.C. Lee, I.T. Kim, and J. Hur, 3D hierarchical structure of MoS_2@G-CNT combined with post-film annealing for enhanced lithium-ion storage, *J. Ind. Eng. Chem.*, 69(2019), p. 116.

[30] Q. Li, G.Z. Zhu, Y.H. Zhao, K. Pei, and R.C. Che, $Ni_xMn_yCo_2O$ nanowire/CNT composite microspheres with 3D interconnected conductive network structure via spray-drying method: A high-capacity and long-cycle-life anode material for lithium-ion batteries, *Small*, 15(2019), No. 15, art. No. 1900069.

[31] H.L. Zhang, C.G. Hu, Y. Ding, and Y. Lin, Synthesis of 1D Sb_2S_3 nanostructures and its application in visible-light-driven photodegradation for MO, *J. Alloys Compd.*, 625(2015), p. 90.

[32] S.J. Wang, S.S. Liu, X.M. Li, C. Li, R. Zang, Z.M. Man, Y.H. Wu, P.X. Li, and G.X. Wang, SnS_2/Sb_2S_3 heterostructures anchored on reduced graphene oxide nanosheets with superior rate capability for sodium-ion batteries, *Chem. Eur. J.*, 24(2018), No. 15, p. 3873.

[33] D.Y.W. Yu, H.E. Hoster, and S.K. Batabyal, Bulk antimony sulfide with excellent cycle stability as next-generation anode for lithium-ion batteries, *Sci. Rep.*, 4(2015), No. 1, art. No. 4562.

[34] J.J. Xie, L. Liu, J. Xia, Y. Zhang, M. Li, Y. Ouyang, S. Nie, and X.Y. Wang, Template-free synthesis of Sb_2S_3 hollow microspheres as anode materials for lithium-ion and sodium-ion batteries, *Nano-Micro Lett.*, 10(2018), No. 1, art. No. 12.

[35] Y.C. Dong, S.L. Yang, Z.Y. Zhang, J.M. Lee, and J.A. Zapien, Enhanced electrochemical performance of lithium ion batteries using Sb_2S_3 nanorods wrapped in graphene nanosheets as anode materials, *Nanoscale*, 10(2018), No. 7, p. 3159.

[36] J. Ren, R.P. Ren, and Y.K. Lv, A flexible 3D graphene@CNT@MoS_2 hybrid foam anode for high-performance lithium-ion battery, *Chem. Eng. J.*, 353(2018), p. 419.

[37] Y.R. Dong, H. Jiang, Z.N. Deng, Y.J. Hu, and C.Z. Li, Synthesis and assembly of three-dimensional MoS_2/rGO nanovesicles for high-performance lithium storage, *Chem. Eng. J.*, 350(2018), p. 1066.

[38] C.R. Zhu, X.H. Xia, J.L. Liu, Z.X. Fan, D.L. Chao, H. Zhang, and H.J. Fan, TiO_2 nanotube@SnO_2 nanoflake core-branch arrays for lithium-ion battery anode, *Nano Energy*, 4(2014), p. 105.

[39] W.J. Tang, X.L. Wang, D. Xie, X.H. Xia, C.D. Gu, and J.P. Tu, Hollow metallic 1T MoS_2 arrays grown on carbon cloth: A freestanding electrode for sodium ion batteries, *J. Mater. Chem. A*, 6(2018), No. 37, p. 18318.